Baltic J. Modern Computing, Vol. 14 (2040), No. 3, pp. 645–668
https://doi.org/10.22364/bjmc.2026.14.3.07

Study of Lagrangian Particle Swarm Algorithm for Cooperative System

Oleh SINKEVYCH, Bohdan SOKOLOVSKII, Yaroslav BOYKO, Igor OLENYCH

Ivan Franko National University of Lviv, Ukraine

{oleh.sinkevych, bohdan.sokolovskyy, yaroslav.boyko, igor.olenych}@lnu.edu.ua

ORCID 0000-0001-9834-2700, 0000-0002-2561-3255, 0000-0001-5967-6345, 0000-0002-6642-0222

Abstract. This paper introduces a study of a physics-inspired extension of the Particle Swarm Optimization algorithm for coordinated particle motion. The method reformulates Particle Swarm foundations within a Lagrangian framework, which allows defining particle motion with each particle possessing physical properties such as mass and size. Attractive and repulsive potential fields, together with a spring–damper interaction model, control the swarm dynamics. Personal and global best positions determine the collective movement of particles toward a target equilibrium region. The proposed potential functions prevent collisions among particles and with obstacles. The model also incorporates Rayleigh dissipation to account for energy loss, and a semi-implicit Euler integration scheme computes the discrete-time motion. Validation in a two-dimensional environment with obstacles demonstrates that the proposed approach results in positive net dissipation, and the energy-aware analysis provides engineers with quantitative metrics for parameter tuning, interaction strength calibration, and performance optimization. The developed framework bridges bio-inspired optimization and classical mechanics, offering both a principled foundation for swarm modeling and a diagnostic toolkit for understanding emergent collective dynamics.

Keywords: Lagrangian dynamics, multi-agent systems, particle swarm optimization, swarm intelligence, physics-inspired algorithms.

1 Introduction

Motion dynamics grounded in nature-inspired metaheuristics and swarm intelligence are widely studied in numerous works (Spears and Spears, 2012; Tzanetos and Dounias, 2017; Yang, 2020; Lu et al., 2025). The principles of coordinated movement observed in the behavior of birds, ants, bees, and flocks form the basis not only for heuristic optimization methods but also complement approaches that model the motion of physical

particles (Olfati-Saber, 2006; Morin et al., 2015; Zhou et al., 2024; Nguyen, 2024). However, most well-established swarm-based algorithms, such as Particle Swarm Optimization (PSO) (Kennedy and Eberhart, 2002; Shami et al., 2022), Ant Colony Optimization (Dorigo et al., 2006; Blum, 2024), and related families of methods are highly abstract, and their derivations do not account for physically consistent aspects. Furthermore, many nature-inspired and physics-inspired optimization algorithms (Biswas et al., 2013) are based on processes found in nature, but they do not attempt to simulate them realistically. Instead, they significantly simplify these processes and keep only basic rules that are useful for computation (Sörensen, 2015; Eiben and Smith, 2015). These shortcomings limit their use in multi-agent motion models that require solid physical foundations and complex interaction rules.

In general, the motion of physical objects is described using Newtonian or Lagrangian dynamics (Wolf Pila, 2019), where motion emerges from forces, constraints, and energy interactions. However, classical physical models do not explicitly incorporate mechanisms of collaborative swarm behavior, such as alignment, cohesion, or flocking (Vicsek et al., 1995). Thus, this leads to a gap between the strict physical determinism of object motion and nature-inspired swarm approaches that explicitly encode collective organization and interaction rules.

Several studies have attempted to bridge this gap. For example, in works (Mikki and Kishk, 2007, 2008), a rethinking of the standard PSO using the basics of molecular dynamics and thermodynamics is proposed in order to combine physical principles with a nature-inspired swarm algorithm. Similarly, the Firefly algorithm (Fister et al., 2013) incorporates simplified physical laws of light propagation, where attractiveness decreases according to the inverse-square law and absorption effects, causing brighter fireflies to attract dimmer ones.

More recent studies have introduced additional physical principles into swarm models. For instance, the Gravitational Search Algorithm (Yang et al., 2022) treats particles as masses attracting via Newton's law; Colliding Body Optimization (Kaveh, 2021) utilizes Newtonian collisions between bodies to exchange momentum for particle velocity updates; Artificial Physics Optimisation (Khan et al., 2025) uses candidate solutions as physical particles with masses proportional to fitness, which interact via virtual gravity-like forces. A more advanced approach comes from (Alvarez-Alvarado et al., 2021), where quantum mechanical equations are used to derive rules for particle interactions.

Taking into account the challenge of combining physically grounded multi-particle dynamics with nature-inspired swarm algorithms, this paper proposes a motion model that integrates Particle Swarm Optimization, Lagrangian dynamics, and the Rayleigh dissipation function. The proposed unified Lagrangian framework describes the coherent motion of a multi-particle system toward a target within a two-dimensional environment containing obstacles. To model collision avoidance between particles and obstacles within the environment, potential-field interactions are incorporated directly into the swarm motion equations. Based on the kinetic and potential energy profiles, along with dissipative components, an approach and metrics for analyzing swarm behavior are proposed. This establishes a physically consistent foundation for future trajectory planning, navigation (Tarihmen et al., 2020), and collective motion methods rooted in both swarm intelligence and classical dynamics.

2 Lagrangian cooperative motion model

Let p_i be a circular particle of radius r_i with mass m_i, velocity vector $\mathbf{v}_i(t) = (v_1, v_2)$, and position $\mathbf{x}_i(t) = (x_1, x_2)$ in two-dimensional space at time step t. The swarm of all particles is defined as $\mathbf{S} = \{p_1, p_2, ..., p_N\}$, where N is the total number of particles. Each particle is initialized within a radius r_s of the starting location $\mathbf{x}_s$, and the initial swarm $\mathbf{S}$ positions are normally distributed in the vicinity of $\mathbf{x}_s$. At every simulation round, particles are placed at random, taking care to ensure they do not overlap or collide with each other.

Particles are intended to move in two-dimensional space from their initial neighborhood of radius r_s to an equilibrium region predefined by the target coordinates $\mathbf{x}_T$. By equilibrium region, we assume particle states where their movement stabilizes around $\mathbf{x}_T$, i.e., in which the system reaches a minimum of its total energy $E_T(t)$, $E_T(t) = U_T(t) + K_T(t)$, where $K_T(t)$ is the swarm's kinetic energy, and $U_T(t)$ is the potential energy at time step t.

To derive the particle movement in the swarm formation, we define the individual particle Lagrangian function $L_i(\mathbf{x}_i, \dot{\mathbf{x}}_i, t)$ as

$$L_i(\mathbf{x}_i, \dot{\mathbf{x}}_i, t) = \frac{m_i ||\dot{\mathbf{x}}_i||^2}{2} - U(\mathbf{x}_i, t) \tag{1}$$

and the total Lagrangian as the sum of individual particle Lagrangians as

$$L(\mathbf{x}_i, \dot{\mathbf{x}}_i, t) = \sum_{i=1}^{N} L_i(\mathbf{x}_i, \dot{\mathbf{x}}_i, t) \tag{2}$$

$U(\mathbf{x}_i, t)$ is the particle's potential, which contains attractive $A(\mathbf{x}_i, t)$ (analogous to a spring-damper system), $T(\mathbf{x}_i, t)$ (target attraction), and a repulsive term $R(\mathbf{x}_i, t)$

$$U(\mathbf{x}_i, t) = A(\mathbf{x}_i, t) + T(\mathbf{x}_i, t) + R(\mathbf{x}_i, t), \tag{3}$$

$$A(\mathbf{x}_i, t) = \frac{c_1}{2} ||\mathbf{x}_i(t) - \mathbf{g}_b(t)||^2 + \frac{c_2}{2} ||\mathbf{x}_i(t) - \mathbf{p}_b(t)||^2, \tag{4}$$

$$T(\mathbf{x}_i, t) = \frac{c_3}{2} ||\mathbf{x}_i(t) - \mathbf{x}_T||^2, \tag{5}$$

$$R(\mathbf{x}_i, t) = R_{ij}(\mathbf{x}_i, \mathbf{x}_j, t) + R_{io}(\mathbf{x}_i, \mathbf{O}, t), \tag{6}$$

where $R_{ij}(\mathbf{x}_i, \mathbf{x}_j, t)$ stands for inter-particle repulsion defined as follows

$$R_{ij}(\mathbf{x}_i, \mathbf{x}_j, t) = \sum_{j=1, i \neq j}^{N} \frac{c_4}{(||\mathbf{x}_i(t) - \mathbf{x}_j(t)||^2 + \epsilon^2)^{\frac{n}{2}}}, \tag{7}$$

and $R_{io}(\mathbf{x}_i, \mathbf{O}, t)$ is the repulsion from obstacles $\mathbf{O}$

$$R_{io}(\mathbf{x}_i, \mathbf{O}, t) = \sum_{o=1}^{N_O} \frac{c_4}{(||\mathbf{x}_i(t) - \mathbf{x}_\mathbf{O}||^2 + \epsilon^2)^{\frac{n}{2}}}, \tag{8}$$

where N_O is the number of nearby obstacles within cutoff radius ρ_0 around the particle position $\mathbf{x}_i$. Here, c_1, c_2, and c_3 are attractive coefficients; c_4 is the weight common to the inter-particle and obstacle repulsion functions; $\mathbf{g}_b(t)$ and $\mathbf{p}_b(t)$ are the global best swarm position and the personal best particle's position, which are determined on the basis of closeness, i.e., Euclidean distance to $\mathbf{x}_T$; ϵ is a small positive regularization parameter; $n > 0$ is the power of repulsion; $\mathbf{x_O}$ is the closest point on the obstacle boundary to the agent position $\mathbf{x}_i$.

The trajectory of a particle is determined by the principle of stationary action, which states that the action defined as the time integral of the Lagrangian $L(\mathbf{x}_i, \dot{\mathbf{x}}_i, t)$ is stationary with respect to small variations of the path. In the presence of dissipative forces, this leads to a modified Euler–Lagrange equation that includes the Rayleigh dissipation term $D(\dot{\mathbf{x}}_i, t) = \frac{1}{2}\gamma||\dot{\mathbf{x}}_i||^2$, and the equations take the form

$$\frac{d}{dt}(\frac{\partial L}{\partial \dot{\mathbf{x}}_i}) - \frac{\partial L}{\partial \mathbf{x}_i} + \frac{\partial D}{\partial \dot{\mathbf{x}}_i} = \mathbf{0}. \tag{9}$$

The Rayleigh term introduces dissipation into the equations of motion, representing the loss of a particle's energy due to damping, and its strength is determined by the parameter γ.

Based on (9), the equation of particle motion is

$$m_i\ddot{\mathbf{x}}_i = -\nabla U(\mathbf{x}_i, t) - \gamma\dot{\mathbf{x}}_i. \tag{10}$$

By substituting (1) and (2) into (10) and applying finite difference schemes

$$\dot{\mathbf{x}}_i \approx \frac{\mathbf{x}_i(t) - \mathbf{x}_i(t - \Delta t)}{\Delta t} = \mathbf{v}_i(t), \ddot{\mathbf{x}}_i \approx \frac{\mathbf{x}_i(t + \Delta t) - 2\mathbf{x}_i(t) + \mathbf{x}_i(t - \Delta t)}{\Delta t^2}, \tag{11}$$

where Δt is the integration step, the rule for updating the unconstrained velocity of an individual particle $\mathbf{v}_i^*(t)$ is expressed as follows:

$$\mathbf{v}_i^*(t + \Delta t) = (1 - \gamma\frac{\Delta t}{m_i})\mathbf{v}_i(t) - \frac{\Delta t}{m_i}\nabla U(\mathbf{x}_i, t) + \boldsymbol{\xi}_i. \tag{12}$$

Here, $\boldsymbol{\xi}_i \sim \mathcal{N}(0, \sigma_i^2\mathbf{I})$ is Gaussian noise introduced to incorporate stochasticity into particle motion, where the standard deviation σ_i is adaptively scaled by the magnitude of the potential force: $\sigma_i = \beta \cdot \frac{\Delta t}{m_i}\|\nabla U(x_i, t)\| \cdot \frac{1}{\sqrt{d}}$, where d is the dimensionality of the space, $\beta \ll \sqrt{d}$ is a small scaling parameter that controls the strength of fluctuations, and $\mathbf{I}$ is the identity matrix.

If the resulting unconstrained velocity vector has a magnitude larger than the predefined v_{max}, $\mathbf{v}_i^*(t + \Delta t)$ is scaled to v_{max}.

In the presence of convex obstacles, a tangential projection matrix $\mathbf{P} = \mathbf{I} - \hat{\mathbf{n}}\hat{\mathbf{n}}^T$ is introduced, where $\hat{\mathbf{n}}$ is the outward unit normal vector to the obstacle boundary at the closest point to the particle position. It is used to remove the normal component of the velocity vector, which, in turn, allows the particle to slide along the boundary. Furthermore, this represents a dissipative force, which decreases the energy of the swarm system. The tangential projection is activated when the particle enters the cutoff radius

ρ and approaches the obstacle ($\mathbf{v}_i^* \cdot \hat{\mathbf{n}} < 0$), which ensures energy dissipation occurs only during boundary approach. Thus, the velocity update rule becomes

$$\mathbf{v}_i(t+\Delta t) = \begin{cases} \mathbf{P}\mathbf{v}_i^*(t+\Delta t), & \text{if } \|\mathbf{x}_i(t) - \mathbf{x}_\mathbf{O}\| \le \rho, \\ \mathbf{v}_i^*(t+\Delta t), & \text{otherwise.} \end{cases} \tag{13}$$

The proposed tangential projection can also be applied to the force vector $\nabla U(\mathbf{x}_i, t)$, which allows the particle to be directed along an edge of the obstacle by the force. Since no extra potential energy is injected into the system, this allows us to study the energy distribution without incorporating any additional complications.

Finally, the particle position is updated as:

$$\mathbf{x}_i(t+\Delta t) = \mathbf{x}_i(t) + \mathbf{v}_i(t+\Delta t)\Delta t. \tag{14}$$

The components of the gradient $\nabla U(\mathbf{x}_i, t)$, which represent the actual forces acting on the particle, are presented below:

$$\nabla A(\mathbf{x}_i, t) = c_1(\mathbf{x}_i(t) - \mathbf{g}_b(t)) + c_2(\mathbf{x}_i(t) - \mathbf{p}_b(t)), \tag{15}$$

$$\nabla T(\mathbf{x}_i, t) = c_3(\mathbf{x}_i(t) - \mathbf{x}_T), \tag{16}$$

$$\nabla R_{ij}(\mathbf{x}_i, \mathbf{x}_j, t) = -nc_4 \sum_{j=1, i\neq j}^{N} \frac{\mathbf{x}_i(t) - \mathbf{x}_j(t)}{(||\mathbf{x}_i(t) - \mathbf{x}_j(t)||^2 + \epsilon^2)^{1+\frac{n}{2}}}. \tag{17}$$

The gradient $\nabla R_{io}(\mathbf{x}_i, \mathbf{O}, t)$ is expressed similarly to $\nabla R_{ij}(\mathbf{x}_i, \mathbf{x}_j, t)$.

In equation (12), the term $w = 1 - \gamma\Delta t/m_i$ is the first-order approximation of the PSO inertia term, which stands for the particle's ability to preserve its velocity across consecutive time steps.

The proposed particle motion model, derived from Lagrangian mechanics, provides the foundation for studying safe and collision-free multi-particle movement in a constrained two-dimensional space.

3 Numerical experiments

To study the proposed approach, we consider a 300×300 two-dimensional environment containing randomly generated obstacles. Obstacles are modeled as static polygons of arbitrary shape, defined by their vertex coordinates. We assume that all obstacles are known a priori; thus, particles do not perform any online sensing or scanning to detect them. Each obstacle $\mathbf{O}$ induces a repulsive field $R_{io}(\mathbf{x}_i, \mathbf{O}, t)$, which influences particle motion within a cutoff radius ρ_0. If a particle reaches the cutoff distance ρ near the obstacle edge, the normal component of the velocity vector $\mathbf{v}_i^*(t+\Delta t)$ is removed and only the tangential part is used to slide along the edge. All simulations are implemented in Python using open-source scientific computing libraries.

For each numerical experiment, we record the swarm's total tracked energy $E_T(t) = K_T(t) + U_T(t)$, where $K_T(t)$ denotes kinetic energy and $U_T(t)$ represents a model-defined potential energy functional. In addition, we track kinetic energy $K_T(t)$, potential energy $U_T(t)$, and performance metrics including success rate, time-to-target, swarm cohesion, minimum safety distances, and path efficiency. In order to study the energy profiles, power dissipation, energy phase portrait, and potential energy dissipation fraction are also provided.

3.1 Experimental setup

For all numerical experiments, the following parameters are set:

1. Number of particles $N \in \{20, 30\}$;
2. All particle masses $m_i = 1$;
3. All particles are of the same size, defined by radius $r_i = 1$;
4. Integration step $\Delta t = 0.01$ is constant over all runs;
5. Repulsion power $n = 2$ and cutoff radius $\rho_0 = 10$ are constant over all runs;
6. Damping coefficient $\gamma = 6$ and regularization parameter $\epsilon = 0.001$;
7. Attractive weights $c_1, c_2, c_3 \in [0, 100]$ and repulsion weights $c_4, c_5 \in [300, 2000]$ are within a defined range of values, since they have a significant effect on the motion dynamics, $\beta = 0.1$ for all runs;
8. The maximum particle velocity is set to $v_{max} = 10$, that is, if the velocity update in (12) produces a vector whose magnitude is larger than $v_{max} = 10$, the vector is re-scaled to the magnitude v_{max}. This limitation may be interpreted as the effect of an additional dissipative force acting on the particle during Δt. Therefore, it is possible to estimate both the work done by this force and its average value;
9. Two map scenarios are defined by the ratio of obstacles to map size: (A) easy (few obstacles, path largely open), (B) advanced (a moderate number of obstacles, path partially constrained).

3.2 Key experiment metrics

To measure and compare motion dynamics within the numerical experiments, the following metrics, along with the energy dynamics $K(t)$ and $U(t)$, are introduced:

a) the success rate, S_r, is defined as the proportion of particles that successfully reach the target region, defined as a circle of radius $r_{\mathbf{x}_T} = 35$ centered at the target position $\mathbf{x}_T$, within at most $max_{steps} = 10,000$ simulation steps;

b) the motion-to-target time t_{final} is the number of time steps required to reach the target area;

c) swarm cohesion, $C(t)$, is defined as

$$C(t) = \frac{1}{N} \sum_{i=1}^{N} ||\mathbf{x}_i(t) - \mathbf{x}_c(t)|| \tag{18}$$

where $\mathbf{x}_c(t)$ is the swarm's centroid;

d) the safety distance $S_d(t)$ is the minimal gap between particle contours

$$S_d(t) = \min_{\forall i \in 1..N} ||\mathbf{x}_i(t) - \mathbf{x}_j(t)|| - (r_i + r_j) \tag{19}$$

e) the path efficiency, P_e, is defined as the ratio of the average full particle path length to the reference diagonal distance, $D_{\mathbf{x}_T}$, from the starting point $\mathbf{x}_s$ to the target $\mathbf{x}_T$

$$P_e = \frac{D_{\mathbf{x}_T}}{\frac{1}{N}\sum_{i=1}^{N}\sum_{t=0}^{T} \|\mathbf{x}_i(t+\Delta t) - \mathbf{x}_i(t)\|} \tag{20}$$

where T is the total number of time steps;

f) the potential-energy dissipation fraction, χ, measures the fraction of the potential energy released during a simulation step that is dissipated after accounting for stochastic energy injection. Let $\Delta U = U(t+\Delta t) - U(t)$ denote the change in the total potential energy of the swarm. The dissipation fraction is then defined as

$$\chi = \frac{\Delta E_{\text{diss}}}{-\Delta U} = \frac{P_{\text{Rayleigh}}\,\Delta t + E_{\text{sliding}} + E_{\text{clip}} - E_{\text{noise}}}{-\Delta U}, \qquad -\Delta U > 0, \tag{21}$$

where

$$P_{\text{Rayleigh}}(t) = \sum_{i=1}^{N} \gamma \|\mathbf{v}_i(t)\|^2, \tag{22}$$

$$E_{\text{sliding}} = \sum_{i=1}^{N} \frac{m_i}{2} \left(\|\mathbf{v}_{i,\text{clip}}\|^2 - \|\mathbf{v}_i(t+\Delta t)\|^2 \right), \tag{23}$$

$$E_{\text{noise}} = \sum_{i=1}^{N} \frac{m_i}{2} \left(\|\mathbf{v}_i^*\|^2 - \|\mathbf{v}_{i,\text{det}}\|^2 \right), \tag{24}$$

$$E_{\text{clip}} = \sum_{i:\ \|\mathbf{v}_i^*\| > v_{\max}} \frac{m_i}{2} \left(\|\mathbf{v}_i^*\|^2 - v_{\max}^2 \right), \tag{25}$$

Here the velocity update of a single step forms the chain $\mathbf{v}_{i,\text{det}} \to \mathbf{v}_i^* \to \mathbf{v}_{i,\text{clip}} \to \mathbf{v}_i(t+\Delta t)$: $\mathbf{v}_{i,\text{det}}$ is the velocity after the deterministic update (damping and conservative potential forces) before the stochastic perturbation; $\mathbf{v}_i^*$ is the unconstrained velocity of (12) after the Gaussian noise has been added; $\mathbf{v}_{i,\text{clip}}$ is the velocity after the $v_{\max}$ rescaling, so that $\|\mathbf{v}_{i,\text{clip}}\| = \min(\|\mathbf{v}_i^*\|, v_{\max})$; and $\mathbf{v}_i(t+\Delta t)$ is the final velocity after the tangential projection of (13).

3.3 Scenario (A) results

This scenario assumes a relatively simple obstacle map geometry (12 obstacles of different shapes) with a largely open path towards the target (Fig. 1). Here, only a few big obstacles are placed in the center of the map, thus, agents aim to find a safe path to the target area while being aware of the repulsion field generated by the obstacles. The visualization of the motion results of 20 particles is shown in Fig. 2.

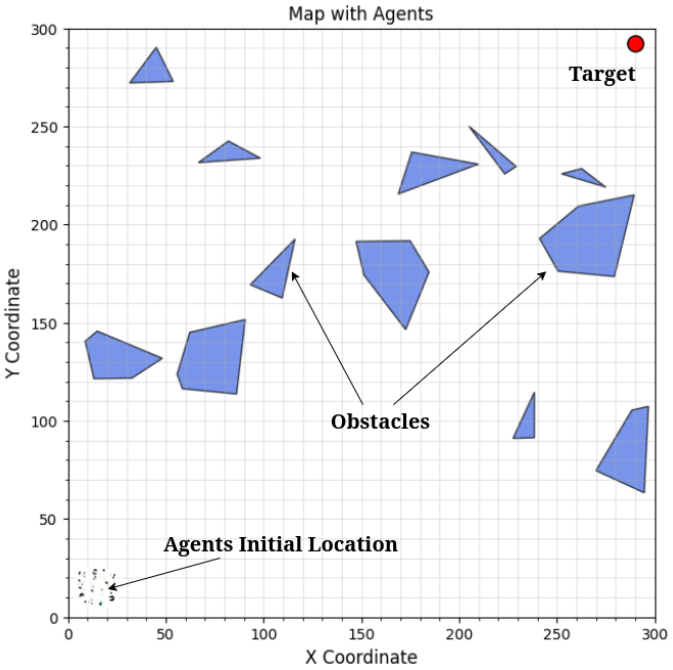

Fig. 1: Map for Scenario (A)

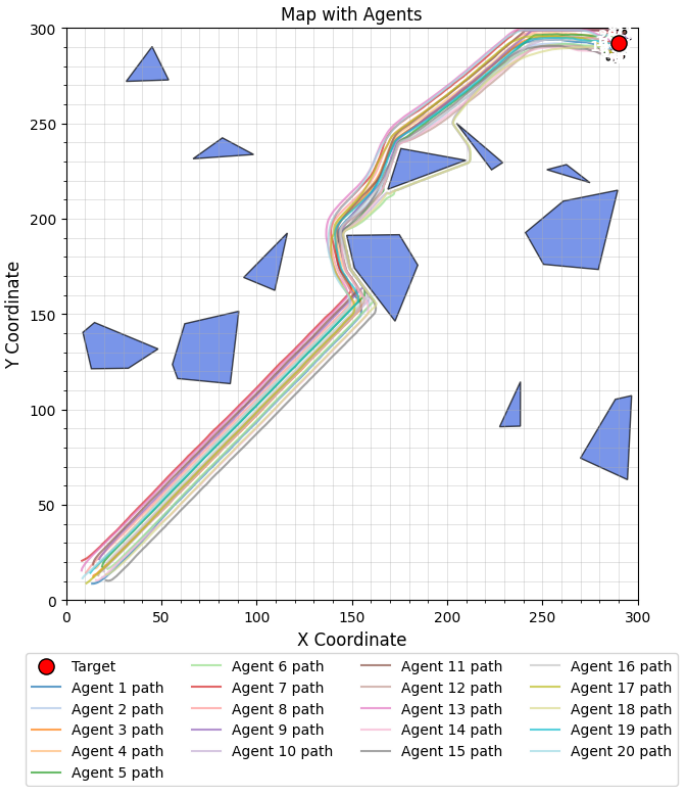

Fig. 2: Agents Trajectories: $N = 20$

To study agent motion, the attractive and repulsion weights were set as $c_1 = c_2 = 15$, $c_3 = 0.2$, $c_4 = 1500$, while the rest of the parameters were kept as described in Section 3.1. Parameters c_1, c_2, c_3, and c_4 were chosen on the basis of numerical experiments to ensure stable swarm motion. Within the current setup, all the particles reached the target area without observed collisions in $t_{final} = 4508$ steps, i.e., the success rate $S_r = 100\%$. The average number of steps among particles to reach the target is 4448. Likewise, during the motion, particles successfully circumvented obstacles by sliding near their edges using repulsive potentials.

During the run, the following metrics were observed: swarm cohesion mean value $C(t) = 6.37$, swarm cohesion median 6.05, swarm cohesion 95th percentile (p95) 7.7 (Fig. 3). Near the largest central obstacles, the swarm of particles showed slightly tighter geometrical organization. However, under the influence of repulsive potentials, to get around the obstacle, the particles stretched, and their cohesion increased. When approaching the target and due to the absence of obstacles, the value of the swarm's cohesion stabilized almost to its value at the beginning of the route.

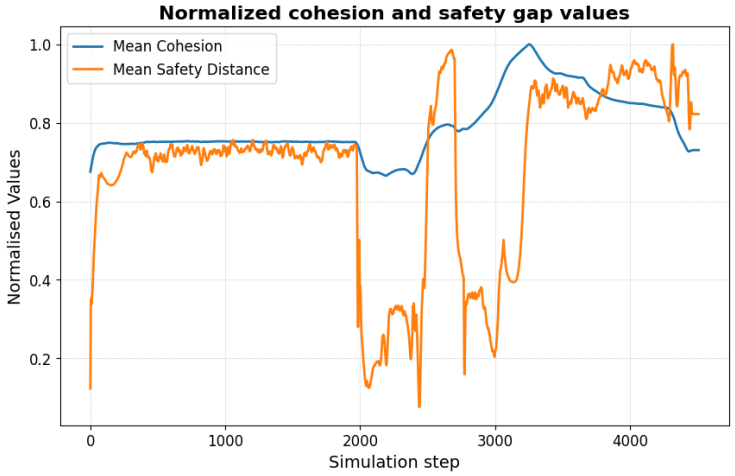

Fig. 3: Normalized Cohesion and Safety Gaps in Scenario (A): $N = 20$

The averaged safety distance demonstrated a more oscillatory behavior with sharp jumps near obstacle surfaces and map boundaries, but overall repeated the cohesion pattern.

A more representative picture of the swarm dynamics can be obtained from the distribution of the normalized energy indicators (Fig. 4a), where each component is normalized by its own maximum absolute value. First, the behavior of the kinetic energy distribution clearly reveals the influence of obstacles, which manifests itself as oscillations in the energy profile beginning near the center of the map caused by Rayleigh dissipation and Gaussian noise injection. These oscillations reflect the effect of dissipative (non-conservative) forces on particle motion. Furthermore, the kinetic energy decreases to nearly zero in the vicinity of the target region, which is consistent with the underlying physical formulation of the model.

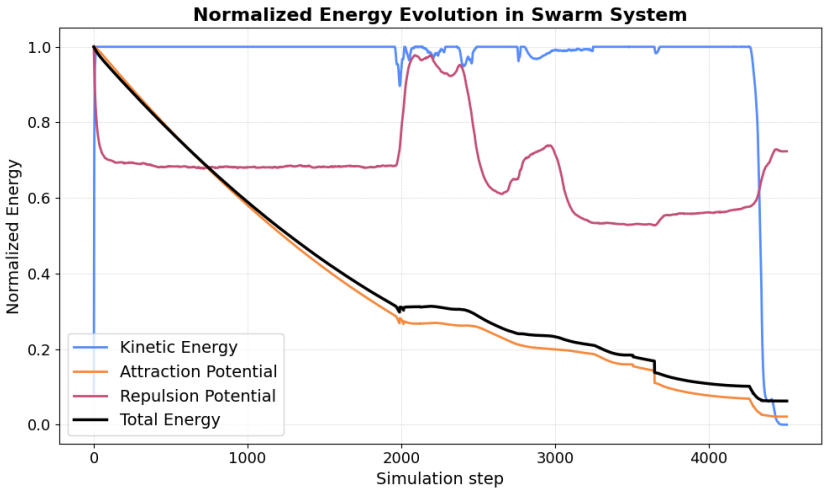

(a) Normalized Energy Evolution

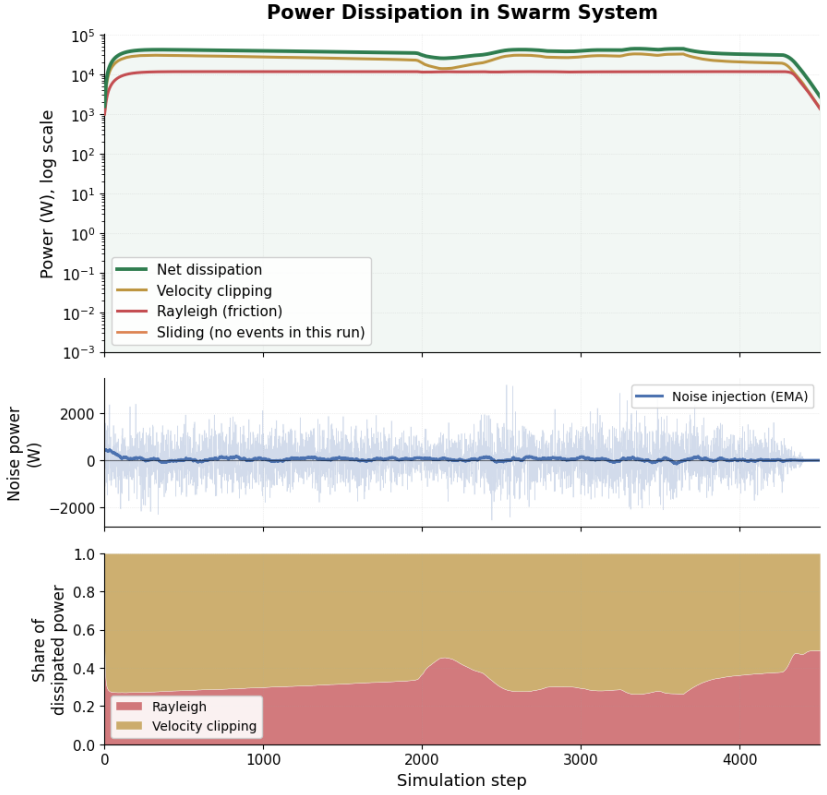

(b) Energy Dissipation Profile

Fig. 4: Scenario (A): $N = 20$

The normalized attraction potential exhibits a clear decreasing trend toward the target area, with small local fluctuations indicating the presence of obstacles and the clustering of particles near their boundaries. The repulsive potential allows for clear repulsion from the obstacles within their reach, which is visible from the central hump. Furthermore, during the movement of particles, the repulsive force between them decreases, but it increases at the end of the movement near the target area, where the particles accumulate. Since the proposed particle-dynamics model includes several non-conservative mechanisms, such as Rayleigh damping, tangential sliding, Gaussian noise, and velocity-limiting effects, the total mechanical energy of the system is not conserved. It is therefore of particular interest to examine the spatial distribution of the scaled dissipative components shown in Fig. 4b.

As illustrated in Fig. 4b, navigating around obstacles induces changes in the system's energy dissipation rate. Rather than indicating systemic instability, these fluctuations reflect rapid, localized energy exchanges driven by the effects of the system's non-conservative mechanisms. Specifically, the bump in the middle of the plot is mostly caused by continuous energy loss via Rayleigh damping, and velocity clipping processes. The spatial distribution of energy dissipation provides valuable insights into the swarm's energy behavior within the potential field. This information can serve as the basis for predictive models that optimize swarm trajectories by incorporating additional energy terms, such as conserved particle energy.

Fig. 5a presents the energy phase portrait of the swarm, where the total potential energy is plotted against the kinetic energy throughout the entire simulation. The trajectory reveals that the swarm rapidly reaches a high-energy state and subsequently evolves along a nearly horizontal branch, which indicates that the kinetic energy remains close to its maximum while the potential energy gradually decreases. A deviation from this regime occurs between approximately 2000 and 3000 simulation steps, where distinct "canyons" appear in the phase trajectory. These features correspond to temporary reductions in kinetic energy and are consistent with the evolution of the dissipation fraction, χ, shown in Fig. 5b. The simultaneous decrease in kinetic energy and increase in χ indicates episodes of enhanced energy dissipation, when the particles entered the obstacle zone. Starting from the middle of the map, a larger fraction of the available kinetic energy is converted into dissipative losses instead of being transformed into particle motion. Occasional negative values of χ correspond to time steps in which the stochastic energy injection temporarily exceeds the dissipative losses. This results in a net gain of kinetic energy from the non-conservative terms.

The energy phase portrait provides a clear view of the swarm dynamics and helps identify changes in its behavior that are difficult to observe from energy time series alone. The nearly horizontal branch indicates a stable motion regime with almost constant kinetic energy, and the local perturbations correspond to short periods of increased energy dissipation and swarm reorganization caused by interactions within the potential field and Gaussian noise.

Increasing the number of particles to $N = 30$ produced slightly different results (Fig. 6). In this setup, due to the larger number of particles and dense formation, five particles became stuck near the obstacles for more than 20 steps, and were eliminated from the simulation.

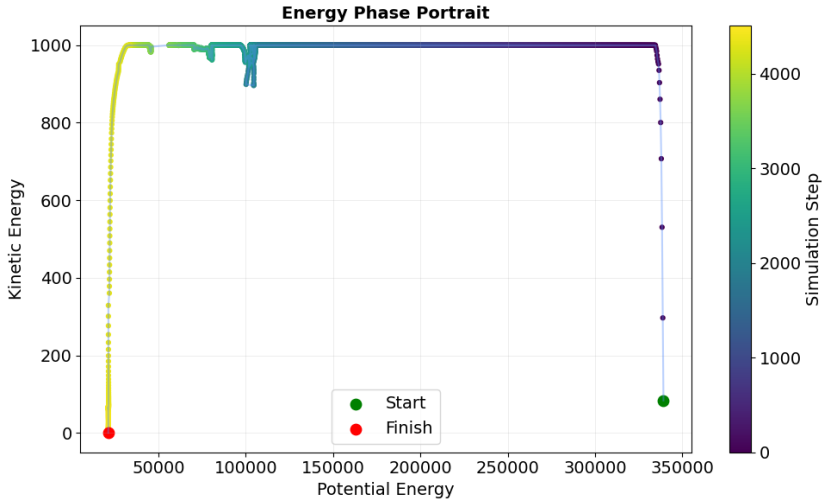

(a) Normalized Kinetic and Potential Energies

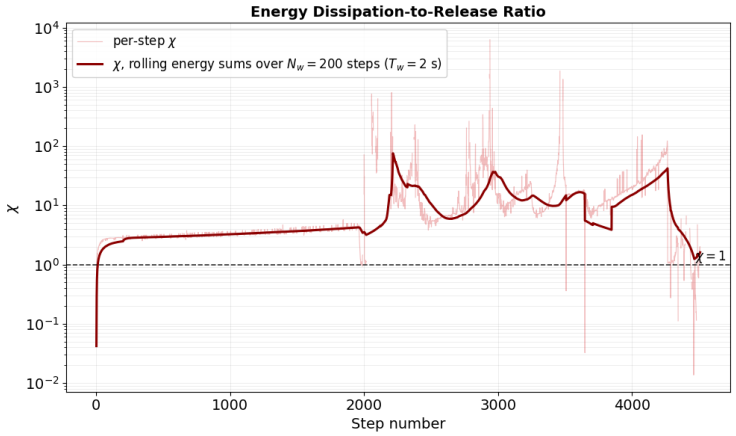

(b) Power Dissipation

Fig. 5: Scenario (A): $N = 20$

Only 25 out of 30 particles reached the target area in 5686 steps; i.e., the success rate $S_r = 83\%$, and their path efficiency value $P_e = 0.97$. Swarm cohesion mean value $C(t) = 13.6$, swarm cohesion median is 10.3, and the 95th percentile (p95) swarm cohesion is 31. Regarding safety gaps during the simulations, the mean safety gap is 0.88, the median safety gap is 0.83, and the 95th percentile (p95) safety gap is 1.16. Normalized cohesion and safe gap values are depicted in Fig. 7. Increasing the swarm size from $N = 20$ to $N = 30$ significantly changed the system's dynamics due to the higher particle density. Because inter-particle repulsion (Eq. 7) is pairwise, the denser swarm amplifies the net repulsive forces on each agent. The larger group also shifts the centroid and global best position $\mathbf{g}_b$, which modifies the attractive forces. Together with

the changed obstacle repulsion forces, these factors drive the particles along distinctly different trajectories. This formation caused five particles to become stuck near the obstacles.

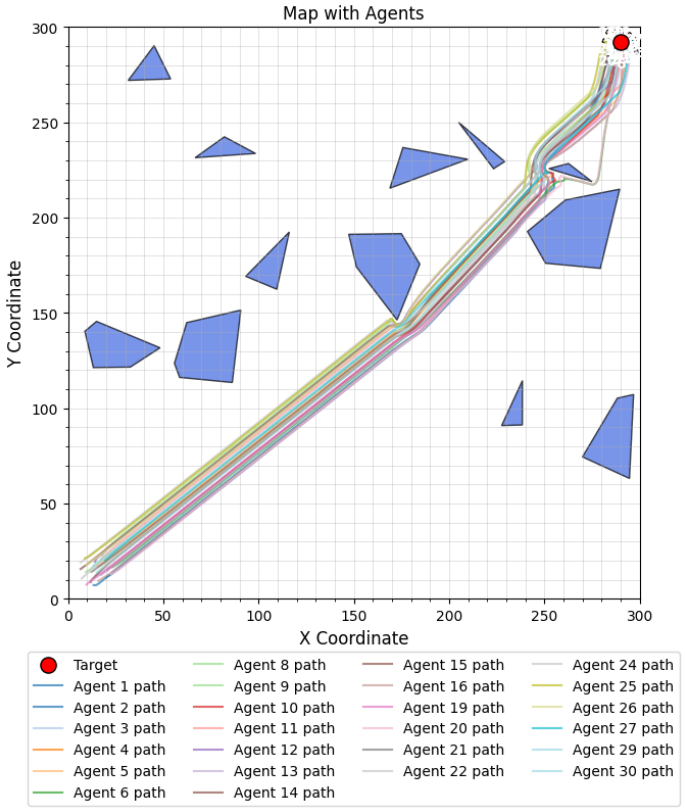

Fig. 6: Agents Trajectories: $N = 30$

In this dense state, the combined repulsion from the obstacle and the swarm behind them creates a local potential minimum, which could not be resolved using only the tangential force and velocity projections, i.e., the tangential and attractive forces guiding the agents toward the target are insufficient to overcome this repulsive barrier, leaving the five particles stuck. Since the swarm operates solely within the configured potential field, with only a small Gaussian noise injection and without incorporating the particles' individual potential energy, this behavior is consistent with the constraints of the model.

The normalized energy profiles and dissipation power are shown in Fig. 8. The kinetic energy profile (Fig. 8a) exhibits several decreases as the swarm passes through obstacle-constrained regions. In these areas, the particles slow down while moving through narrow passages and accelerate again after leaving them. The attraction potential gradually increases after approximately step 2000, when the swarm reaches the central obstacle, and reaches a maximum near step 4000 as the particles approach the

target region. This increase occurs because the obstacle prevents the particles from moving directly toward their cognitive and social attractors, which causes deviations from their preferred trajectories. After passing the obstacle, the repulsion potential decreases as the initially compact swarm stretches along the obstacle boundary. The resulting increase in the average distance between neighboring particles reduces the overall repulsive interaction energy.

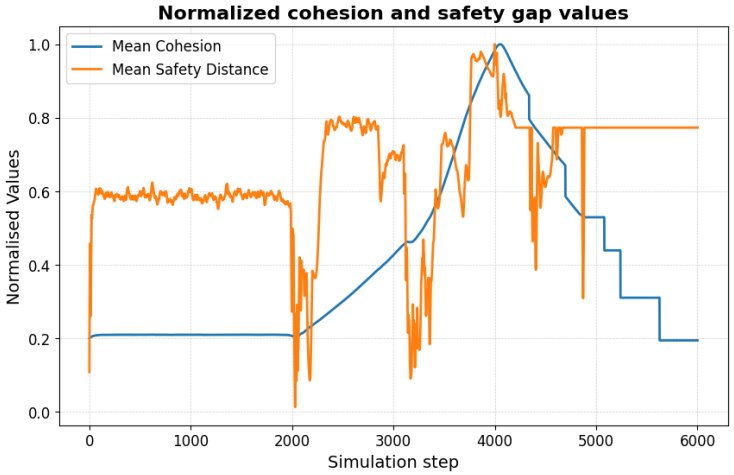

Fig. 7: Normalized Cohesion and Safety Gaps in Scenario (A): $N = 30$

In Fig. 8b, the dissipation power shows how the interaction with obstacles affects the energy losses of the swarm. The sliding dissipation increases when the particles move along the boundary of the final triangular obstacle, which indicates active contact between the swarm and the obstacle surface. After leaving the contact region, the sliding contribution rapidly decreases. During most of the simulation, velocity clipping accounts for the largest part of the energy dissipation. The contribution from Rayleigh damping decreases as the particle velocities become lower during the final stages of convergence. The increase in noise power during the obstacle interaction partially compensates for the dissipative losses, reducing the net dissipation rate in this region.

Fig. 9a demonstrates a more intricate kinetic-potential behavior than that observed for $N = 20$ particles. From step 4000 onward, the swarm rapidly moves toward the target without hitting obstacles, causing both kinetic and potential energy to steadily decrease. In contrast, when navigating near obstacles, the dense swarm formation causes potential energy to rise while kinetic energy drops. The loops in the phase portrait show that the swarm first slows down and builds up tension, then releases it as it squeezes through the walls. In Fig. 9b, the dissipation fraction χ shows how the energy released from the potential field is distributed between particle motion and non-conservative losses. Higher values of χ indicate that a larger fraction of the released potential energy is dissipated rather than converted into kinetic energy. Such regions typically correspond to stronger interactions with obstacles, where particle motion is restricted by sliding and velocity constraints.

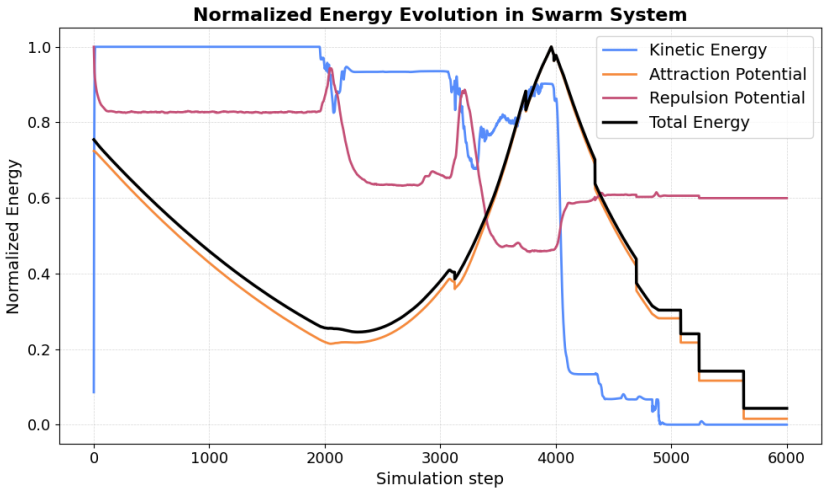

(a) Normalized Kinetic and Potential Energies

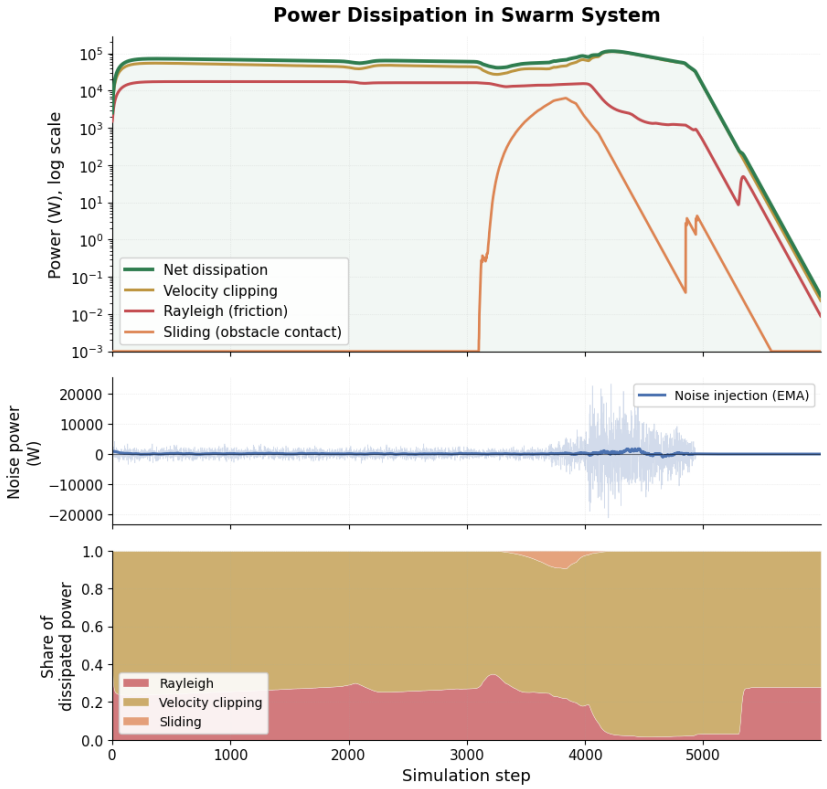

(b) Power Dissipation

Fig. 8: Scenario (A): $N = 30$

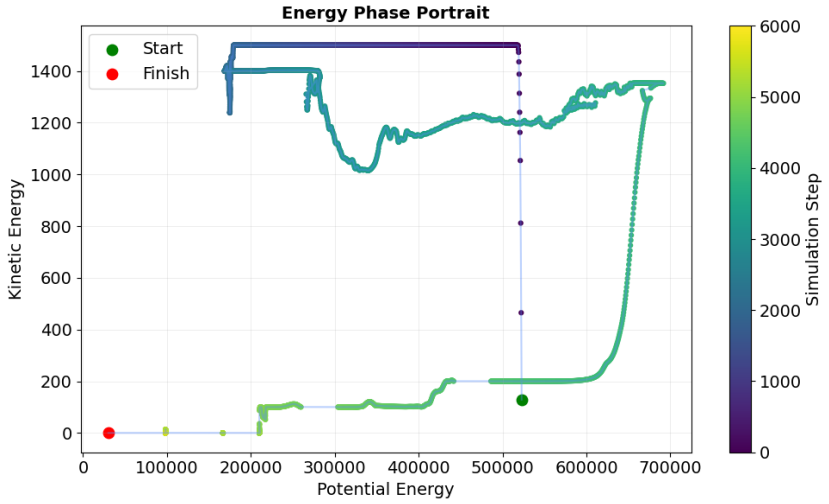

(a) Kinetic and Potential Energies

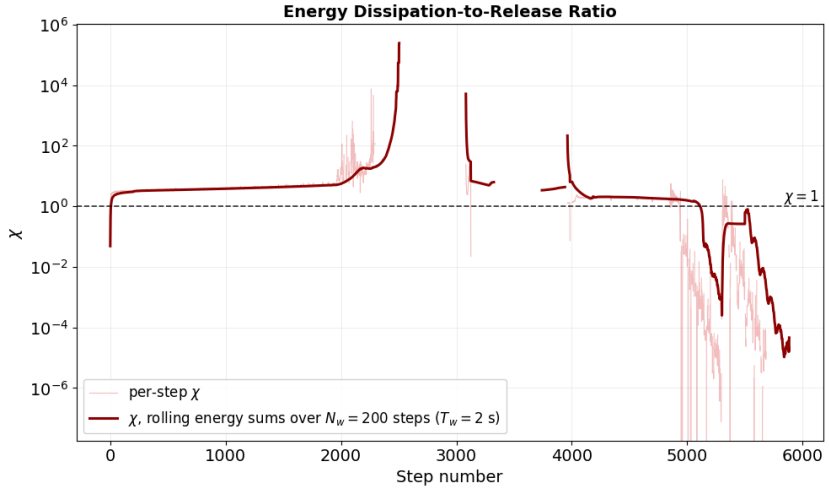

(b) Dissipation Fraction

Fig. 9: Scenario (A): $N = 30$

The value of χ is evaluated only when the potential energy decreases, since the ratio requires a positive amount of released potential energy for normalization. Therefore, gaps in the time series correspond to periods when the swarm accumulates potential energy, for example, when particles are compressed near obstacles. The occasional sharp peaks in χ appear when the change in potential energy approaches zero. Since the dissipated energy remains finite while the released potential energy becomes very small, the ratio increases significantly. These peaks therefore reflect a regime of low energy release rather than exceptionally high dissipation.

It should be noted that in the case of 30 particles, jamming near obstacles occurred only in the configuration specified in the setup of Scenario (A). However, when the weight of c_4 was doubled to 4000, the swarm reached the target area in its entirety. Increasing the repulsive potential in a given configuration of obstacles within the proposed model allows the swarm of particles to reach the target without jamming or inter-particle collisions.

3.4 Scenario (B) results

In this scenario, the number of obstacles (from 12 to 24) and complexity of the map are increased, the path to the target area becomes cluttered, which in turn significantly complicates the movement of particles in the potential field. On the right-center side of the map, there are relatively thin tunnels and a large obstacle, which obscures the target area. For this simulation, due to the more complex obstacles, the number of particles is set to $N = 20$, and the repulsion weight is increased to $c_4 = 5000$.

The resulting particle trajectories are shown in Fig. 10. As seen in Fig. 10, particles struggled to squeeze into the narrow tunnel between two obstacles at coordinates (90, 40). Nevertheless, they all managed to pass through the corridor and continued their motion toward the target. Finally, after a few detours near coordinates (240, 150) and (270, 200), all 20 particles reached the target area with a success rate $S_r = 100\%$ in $t_{final} = 5362$ steps. Among all surviving particles, the average time steps to reach the target is 5081, and the resulting path efficiency value is $P_e = 0.83$.

The current simulation produced a swarm cohesion mean value $C(t) = 11.6$, a swarm cohesion median value of 12.2, and a 95th percentile (p95) swarm cohesion value of 16.6. The increase of the particle repulsion weight c_4 from 1500 to 5000 resulted in overall larger cohesion, whereas the swarm maintained cohesive motion during the whole run. The mean, median, and 95th percentile (p95) safety gaps are 1.84, 1.73, and 2.67, respectively. The normalized mean cohesion and safety gap values are presented in Fig. 11. The circumvention of obstacles under the combined action of attractive and repulsive forces causes particles to become spatially separated during their relative motion, resulting in increased cohesion.

The energy profiles are shown in Fig. 12. The kinetic energy profile shows a distinct drop in the vicinity of step 900, which indicates the presence of nearby obstacles (Fig. 12a). As particles moved through the narrow passage between the obstacles, their velocity continuously increased as they approached the end of the tunnel. The remaining jumps in values are explained by the repulsion of obstacles.

Under the increased repulsive force exerted by the obstacles within the tunnel, the particles were compressed from both sides, while the attractive force toward the target stretched their configuration, giving rise to an attractive potential. Then, it gradually decreased during their movement toward the target. However, a slight increase in attractive potential was observed in the vicinity of the last three obstacles.

Almost all power dissipation of the swarm is explained by Rayleigh dissipation and velocity clamping (Fig. 12b); no sliding dissipation was observed during the simulation. The deceleration of the particles within the narrow passage between the two obstacles reduced the average swarm velocity, which led to a sharp decrease in Rayleigh dissipative power.

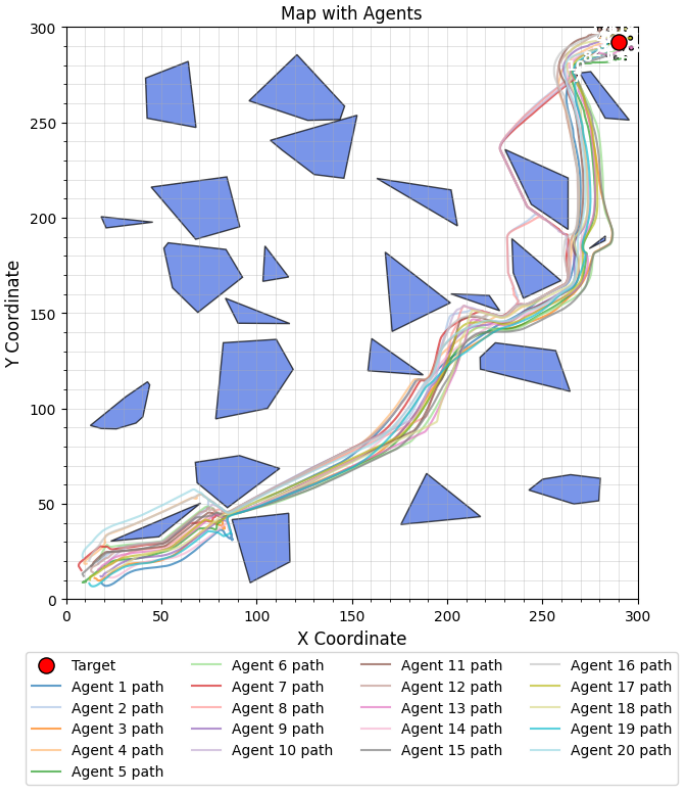

Fig. 10: Agents Trajectories: $N = 20$

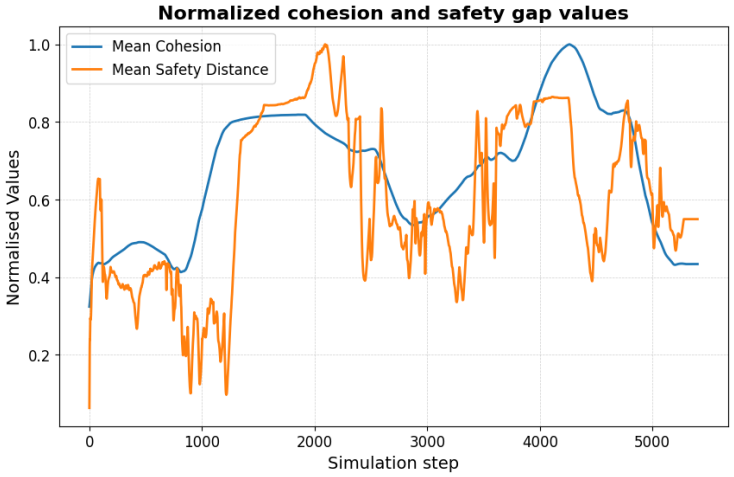

Fig. 11: Normalized Cohesion and Safety Gaps in Scenario (B): $N = 20$

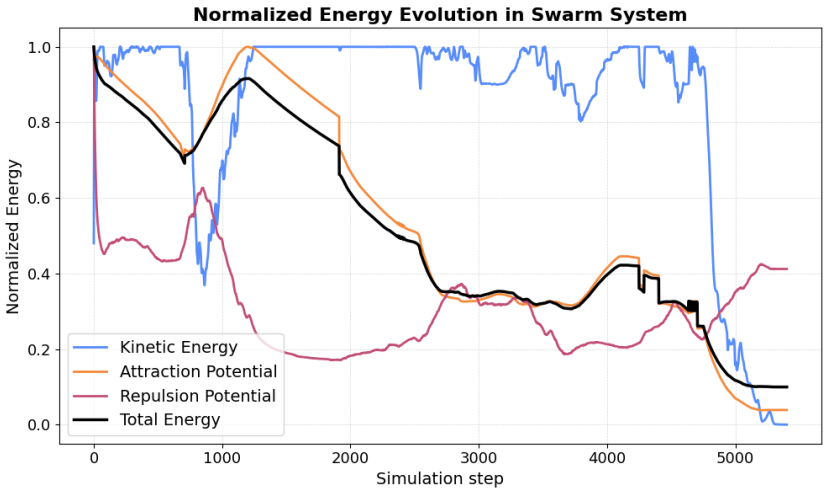

(a) Normalized Kinetic and Potential Energies

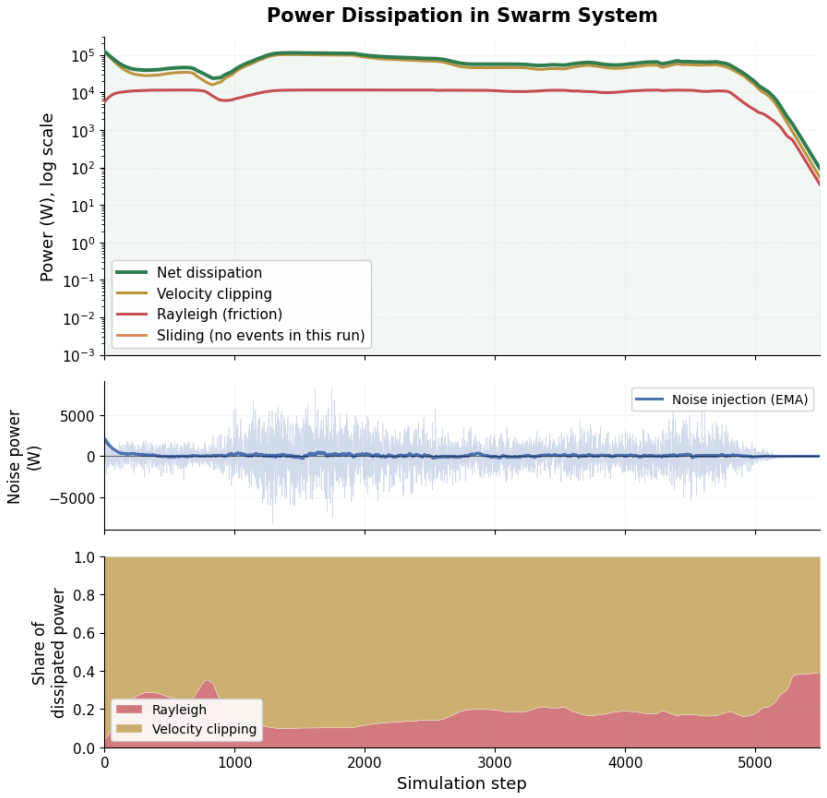

(b) Power Dissipation

Fig. 12: Scenario (B): $N = 20$

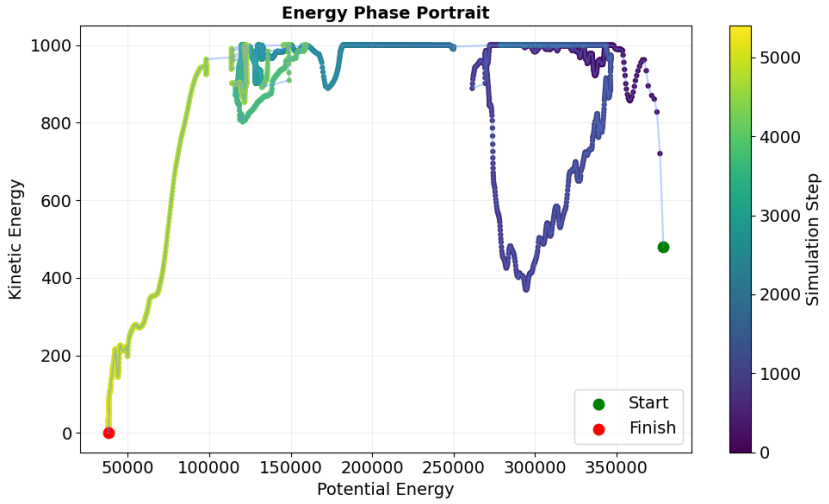

(a) Kinetic and Potential Energies

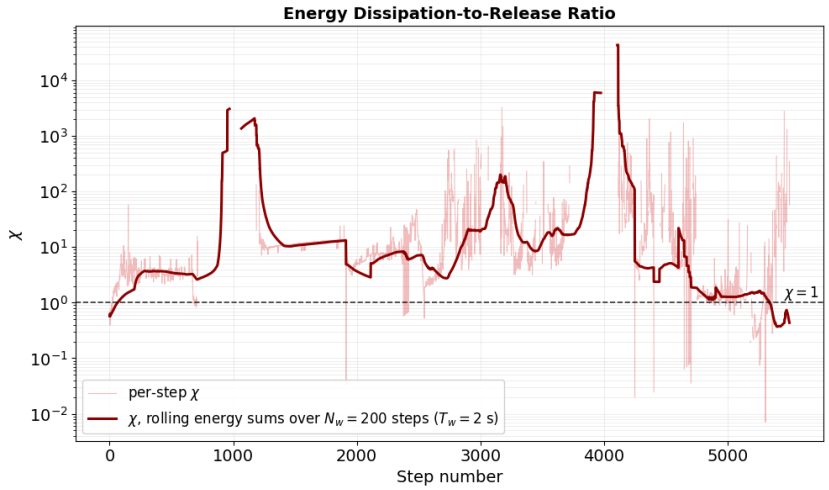

(b) Dissipation Fraction

Fig. 13: Scenario (B): $N = 20$

The kinetic-potential energy profile is presented in Fig. 13a. A significant drop in kinetic energy accompanied by a relatively subtle increase in the potential term indicates particle braking near the obstacles. This behavior, along with the corresponding variations in kinetic and potential energies, is associated with rapid acceleration toward the target and a temporary increase in inter-particle distances (Fig. 11). A similar picture can be observed between steps 3500 and 4000, but with much lower intensity. Then, the swarm consistently continued its motion to the target area, until the total potential energy drops to a minimal value.

The large peaks observed in the dissipation fraction plot (Fig. 13b) are attributed to persistent attraction–repulsion fluctuations, causing particles to oscillate due to the high repulsion weight. Compared to simulations with a lower repulsion weight $c_4 = 1500$, where such pronounced peaks are absent, a higher value of $c_4 = 5000$ leads to unstable and inefficient particle motion and reduces the overall effectiveness of the swarm. These observations suggest that, to ensure more stable and effective swarm motion, the attraction–repulsion weights c_1, c_2, c_3, and c_4 should be adapted according to the geometry of the environment rather than kept constant.

4 Discussion of results

The mathematical model presented in this study has been developed to investigate the motion of particles as a cohesive group or an intelligent swarm formation. To establish the foundation of this study, the particles were considered as physical objects with unit mass moving in a potential field, with a small noise injection introduced to produce slight stochastic behavior. The model derivations are based on the Lagrangian framework, which enables the incorporation of detailed energy terms, including kinetic, potential, and dissipative components. Using the Euler-Lagrange and Rayleigh dissipation equations, a particle motion model has been introduced. To properly incorporate swarm behavior, representing cohesive and purposeful movement, Particle Swarm Optimization concepts were applied as part of the potential functions. Collision avoidance between particles, as well as with obstacles, was implemented using a repulsive potential field. The study of particle motion was conducted on two-dimensional maps containing convex polygonal obstacles, which had to be avoided in order to reach a predefined target region.

The qualitative and quantitative analysis of swarm motion is based on measures of cohesion, minimum inter-particle spacing, path efficiency, and the distribution of energy components, including dissipative losses. In addition, the dissipation fraction, defined as the proportion of the potential energy released that is dissipated through non-conservative mechanisms, is used to evaluate the energy efficiency of the swarm motion.

The study of the developed model results in the following contributions:

1. A hybrid Lagrangian-based framework for swarm particle motion is proposed, establishing an energy-based formulation that provides a rigorous physical description of the system dynamics. Particle Swarm Optimization concepts were utilized to build a physically-inspired swarm motion model.
2. The proposed model incorporates both conservative and non-conservative forces through the Lagrangian formalism and generalized forces, allowing systematic analysis of their effects on particle motion and the overall swarm behavior.
3. The integration of repulsive potentials into the Lagrangian framework enables the particle swarm not only to converge toward the target region while effectively preventing collisions and particle tunneling, but also to successfully avoid obstacles encountered along its trajectory.

4. A set of motion quality metrics is proposed to assess swarm behavior in terms of formation geometry, trajectory characteristics, and the temporal evolution of the swarm's kinetic and potential energies.
5. The temporal profiles of kinetic energy, potential energy, and dissipated power provide insights into the quality of the model configuration. In particular, oscillatory behavior and transient disturbances reveal an imbalance between the attractive and repulsive potential fields, which indicates suboptimal parameter tuning.
6. The power dissipation profile quantifies the contributions of Rayleigh dissipation, velocity clamping, stochastic noise injection, and tangential sliding along obstacle boundaries to the overall energy dissipation of the swarm dynamics.
7. The energy dissipation fraction measures the fraction of released potential energy that is irreversibly dissipated by non-conservative mechanisms. This metric provides a direct measure of the energetic efficiency of the proposed model and serves as an indicator of suboptimal parameters.
8. Given a known obstacle map and the current parameters of the swarm particle motion model, the energy profiles provide the information required to adaptively tune the coefficients c_1, c_2, c_3, and c_4 by solving an optimization problem formulated to minimize mechanical work and irreversible energy losses.

5 Conclusions

This paper is devoted to studying a particle swarm as a mechanical system rather than as an abstract optimization heuristic. First, swarm behavior is described using quantities with a clear physical foundation. Classical PSO-style methods are typically evaluated only on whether the swarm reaches the goal. The energy-based formulation shows how efficiently it arrives there: how much of the released potential energy went into useful motion, how much was lost, and through which mechanisms. Second, the energy profiles aid in diagnostics. Oscillations in kinetic energy, non-efficient exchange between energy components, or a high dissipation fraction all indicate a poor balance between the attractive and repulsive fields. These signs can appear in the energy plots before issues such as particle escape or trapping appear in the trajectories.

This has practical implications for parameter selection. Instead of tuning the coefficients c_1, c_2, c_3, and c_4 by trial and error, the process can be formulated as an optimization problem: for a given map, find the parameters that minimize mechanical work and irreversible energy losses. The model has one clear limitation. Each particle has an unlimited energy supply, which means that all particles can move within the potential field without energy depletion. The latter is not the case for real-world robotic swarm systems. Adding a finite energy reservoir to each particle will be the next step in future research, along with testing the model in more complex environments where obstacles are non-convex and contain blind corners. In addition, incorporating a Hamiltonian function could qualitatively complement this study.

References

Alvarez-Alvarado, M. S., Alban-Chacón, F. E., Lamilla-Rubio, E. A., Rodríguez-Gallegos, C. D., Velásquez, W. (2021). Three novel quantum-inspired swarm optimization algorithms using

different bounded potential fields, *Sci. Rep.* **11**(1), 11655. DOI: 10.1038/s41598-021-90847-7.

Biswas, A., Mishra, K. K., Tiwari, S., Misra, A. K. (2013). Physics-inspired optimization algorithms: A survey, *J. Optim.* **2013**, 1–16. DOI: 10.1155/2013/438152.

Blum, C. (2024). Ant colony optimization: A bibliometric review, *Phys. Life Rev.* **51**, 87–95. DOI: 10.1016/j.plrev.2024.09.014.

Dorigo, M., Birattari, M., Stutzle, T. (2006). Ant colony optimization, *IEEE Comput. Intell. Mag.* **1**(4), 28–39. DOI: 10.1109/MCI.2006.329691.

Eiben, A. E., Smith, J. E. (2015). *Introduction to evolutionary computing*, Natural Computing Series, 2 edn, Springer, Berlin, Germany. DOI: 10.1007/978-3-662-44874-8.

Fister, I., Fister, Jr, I., Yang, X.-S., Brest, J. (2013). A comprehensive review of firefly algorithms, *Swarm Evol. Comput.* **13**, 34–46. DOI: 10.1016/j.swevo.2013.06.001.

Kaveh, A. (2021). Colliding bodies optimization, *Advances in Metaheuristic Algorithms for Optimal Design of Structures*, Springer International Publishing, Cham, pp. 209–248. DOI: 10.1007/978-3-030-59392-6_7.

Kennedy, J., Eberhart, R. (2002). Particle swarm optimization, *Proceedings of ICNN'95 - International Conference on Neural Networks*, IEEE. DOI: 10.1109/ICNN.1995.488968.

Khan, A., Liping, X., Bashir, K., Iqbal, N., Hayat, A., Abidin, S. U. (2025). Hybrid Dual-Population artificial physics optimization for complex constrained multi-objective scenarios, *ejaset* **3**(4), 242–255. DOI: 10.59324/ejaset.2025.3(4).20.

Lu, J., Zhao, J., Niu, J. (2025). Boids-based integration algorithm for formation control and obstacle avoidance in unmanned aerial vehicles, *Machines* **13**(4), 255. DOI: 10.3390/machines13040255.

Mikki, S. M., Kishk, A. A. (2007). Physical theory for particle swarm optimization, *Electromagn. Waves (Camb.)* **75**, 171–207. DOI: 10.2528/PIER07051502.

Mikki, S. M., Kishk, A. A. (2008). Particle swarm optimization: A physics-based approach, *Synth. Lect. Comput. Electromagn.* **3**(1), 1–103. DOI: 10.1007/978-3-031-01704-9.

Morin, A., Caussin, J.-B., Eloy, C., Bartolo, D. (2015). Collective motion with anticipation: flocking, spinning, and swarming, *Phys. Rev. E Stat. Nonlin. Soft Matter Phys.* **91**(1), 012134. DOI: 10.1103/PhysRevE.91.012134.

Nguyen, L. V. (2024). Swarm intelligence-based multi-robotics: A comprehensive review, *AppliedMath* **4**(4), 1192–1210. DOI: 10.3390/appliedmath4040064.

Olfati-Saber, R. (2006). Flocking for multi-agent dynamic systems: Algorithms and theory, *IEEE Trans. Automat. Contr.* **51**(3), 401–420. DOI: 10.1109/TAC.2005.864190.

Shami, T. M., El-Saleh, A. A., Alswaitti, M., Al-Tashi, Q., Summakieh, M. A., Mirjalili, S. (2022). Particle swarm optimization: A comprehensive survey, *IEEE Access* **10**, 10031–10061. DOI: 10.1109/ACCESS.2022.3142859.

Sörensen, K. (2015). Metaheuristics-the metaphor exposed, *Int. Trans. Oper. Res.* **22**(1), 3–18. DOI: 10.1111/itor.12001.

Spears, W. M., Spears, D. F. (eds) (2012). *Physicomimetics*, 2012 edn, Springer, Berlin, Germany. DOI: 10.1007/978-3-642-22804-9.

Tarihmen, B., Diyarbakirli, B., Kanbur, M. O., Demirel, H. (2020). Indoor navigation system of faculty of civil engineering, itu: A BIM approach, *Baltic Journal of Modern Computing* **8**(2), 359–369. DOI: 10.22364/bjmc.2020.8.2.11.

Tzanetos, A., Dounias, G. (2017). Nature inspired optimization algorithms related to physical phenomena and laws of science: A survey, *Int. J. Artif. Intell. Tools* **26**(06), 1750022. DOI: 10.1142/S0218213017500221.

Vicsek, T., Czirók, A., Ben-Jacob, E., Cohen, I, I., Shochet, O. (1995). Novel type of phase transition in a system of self-driven particles, *Phys. Rev. Lett.* **75**(6), 1226–1229. DOI: 10.1103/PhysRevLett.75.1226.

Wolf Pila, A. (2019). *Introduction to Lagrangian dynamics*, 2020 edn, Springer Nature, Cham, Switzerland. DOI: 10.1007/978-3-030-22378-6.

Yang, X.-S. (ed.) (2020). *Nature-inspired computation and swarm intelligence*, Academic Press, San Diego, CA. DOI: 10.1016/C2019-0-00628-0.

Yang, Z., Cai, Y., Li, G. (2022). Improved gravitational search algorithm based on adaptive strategies, *Entropy (Basel)* **24**(12), 1826. DOI: 10.3390/e24121826.

Zhou, Y., Wang, T., Wang, T., Lei, X., Peng, X. (2024). Anticipation promotes the velocity alignment in collective motion, *Physica A* **637**(129601), 129601. DOI: 10.1016/j.physa.2024.129601.

Received July 10, 2026 , accepted September 3, 2026